IEEE Access
Multidisciplinary | Rapid Review | Open Access Journal

Received March 21, 2020, accepted April 10, 2020, date of publication April 14, 2020, date of current version April 30, 2020.

Digital Object Identifier 10.1109/ACCESS.2020.2987858

Cross-Section Bead Image Prediction in Laser Keyhole Welding of AISI 1020 Steel Using Deep Learning Architectures

SEHYEOK OH AND HYUNGSON KI

Department of Mechanical Engineering, Ulsan National Institute of Science and Technology (UNIST), Ulsan 44919, South Korea

Corresponding author: Hyungson Ki (hski@unist.ac.kr)

This work was supported by the Basic Science Research Program through the National Research Foundation (NRF) of Korea funded by the Ministry of Science and ICT under Grant NRF-2019R1A2C2089114.

ABSTRACT A deep learning model was applied for predicting a cross-sectional bead image from laser welding process parameters. The proposed model consists of two successive generators. The first generator produces a weld bead segmentation map from laser intensity and interaction time, which is subsequently translated into an optical microscopic (OM) image by the second generator. Both generators exhibit an encoder–decoder structure based on a convolutional neural network (CNN). In the second generator, a conditional generative adversarial network (cGAN) was additionally employed with multiscale discriminators and residual blocks, considering the size of the OM image. For a training dataset, laser welding experiments with AISI 1020 steel were conducted on a large process window using a 2 KW fiber laser, and a total of 39 process conditions were used for the training. High-resolution OM images were successfully generated, and the predicted bead shapes were reasonably accurate (R-Squared: 89.0% for penetration depth, 93.6% for weld bead area).

INDEX TERMS Laser welding, weld-bead prediction, deep learning, image-to-image translation.

I. INTRODUCTION

In recent decades, laser welding has been actively applied to the high-precision joining of metal parts in the automotive, electronics, aerospace, shipbuilding, and medical industries. Laser welding demonstrates high strength, narrow and deep bead shapes, but input laser processing parameters (such as laser power and beam scanning speed) must be carefully selected to achieve the desired weld bead, as the weld bead properties (shape, heat affected zone, microstructures, porosity, etc.) substantially affect the key mechanical properties such as tensile strength, ductility, hardness and fatigue [1]. Therefore, a reliable predictive model is essential, especially for challenging welding applications.

Many researchers have endeavored to establish a good predictive model, as laser welding has become increasingly in demand for a variety of cutting-edge technologies. Lankalapalli *et al.* [2] developed a penetration depth predictive model in terms of laser power and Péclet number, by solving a two-dimensional heat conduction equation with a conical keyhole shape assumption. Lampa *et al.* [3] predicted the penetration depth and weld width using a simplified thermal model, by introducing an effective thermal conductivity considering thermocapillary flow. Chang and Na [4] proposed a new volumetric heat source equation and analyzed the effect of heat source descriptions in laser micro welding. Ki *et al.* [5], [6] developed a self-consistent laser keyhole welding model by considering various physical phenomena at the liquid-vapor interface. Benyounis *et al.* [7] conducted a response surface methodology analysis to achieve correlations for the weld bead geometry in terms of laser power, scanning speed, and focal point position. Hann *et al.* [8] reported a simple physical model to predict the melt depth and width using mean surface enthalpy values. Volpp and Vollertsen [9] established an analytical model of multiple reflections, based on a ray tracing method. Using the two types of beam profiles, keyhole shapes were predicted and compared to the experimental results. Courtois *et al.* [10] developed a laser keyhole welding model using COMSOL Multiphysics® software, and they considered the interaction

The associate editor coordinating the review of this manuscript and approving it for publication was Kok Lim Alvin Yau.

This work is licensed under a Creative Commons Attribution 4.0 License. For more information, see https://creativecommons.org/licenses/by/4.0/

of laser beam and melt pool using the Maxwell equations. Kim and Ki [11] presented a simple scaling law for predicting penetration depth according to laser processing parameters by considering the strength of multiple reflections. Suder and Williams [12] reported an empirical model for predicting penetration depth in terms of laser power, interaction time, and beam diameter. Fabbro [13] studied a scaling law regarding the keyhole depth based on thermal dimensionless parameters. While most of the referenced studies have been useful, they normally require high computational cost with a long computation time and the focus was primarily limited to the geometrical shape of the bead (mostly penetration depth).

In this study, for the first time, a novel deep learning framework was proposed for predicting optical microscopic (OM) image of the cross-sectional laser weld bead, from only two laser processing parameters (laser intensity I_0 and beam interaction time t_i). Our deep learning model can predict the weld bead in real image, i.e. including keyhole, heat affected zone, substrate, microstructures, porosity as well as the geometrical bead shape, which synthetically determine the mechanical properties and weld quality. Also, it can instantly generate multiple predictive bead images in a few seconds from the given input laser process conditions once training ends, so is very handy as well as practical (one can also share the trained model online, using the open source deep learning libraries such as TensorFlow and PyTorch on GitHub). Note that several approaches [14]–[16] using an artificial neural network (ANN) have been reported in bead shape prediction in laser welding, however, to the best of the authors' knowledge, no deep learning model has been reported yet.

The proposed deep learning model is composed of two successive generators, because prediction of such a high-resolution OM image using only one generator is a tough job (the information contained in the input laser process conditions is very limited to generate the OM image). In the first generator, an encoder–decoder network [17] based on a convolutional neural network (CNN) [18] was adopted that converts the input laser processing parameters into a weld bead segmentation map. In the second generator, for a guided high-resolution OM image synthesis, pix2pixHD [19] was adopted. It was basically a CNN-based encoder–decoder on a conditional generative adversarial network (cGAN) [20], [21] frame, with multi-scale generators and discriminators, and deep residual network [22], [23] which is the structure widely used in a super-resolution (SR) problem [24]–[28]; thus, the input segmentation map was filled and exhibited a high-resolution OM image resembling a real image. The work methodology to apply the presented artificial intelligence (AI) model can be summarized in the following three steps: a) collects raw data from the welding experiments on the target material, with various laser process conditions; b) properly augments the raw data and trains the proposed deep learning model; c) validates the model and checks the performance of the model using the test dataset. In this study, at first, the datasets were obtained from laser welding experiments with AISI 1020 carbon steel using a 2 KW multi-mode fiber laser on a large process window. Then, the datasets were augmented using several image processing techniques, and used for the model training. After model validation, performance of the model was tested using a test dataset. Specifically, accuracies for the penetration depth (89.0%) and weld bead area (93.6%) were calculated, and quality of the predicted OM images was assessed.

In summary, the major contributions in this study are as follows.

- A novel deep learning framework was presented for predicting high-resolution cross-section weld bead images in laser welding, from two laser processing parameters (laser intensity and beam interaction time).
- Two individual generators were developed, instead of direct mapping from the input laser process conditions to the high-resolution optical microscopic image, for a stable and semantic learning. A proper data setup method was also proposed accordingly.
- An optimal model structure suitable for the weld bead image prediction was proposed, obtained from the processes of validation and trial and errors. Also, inside of the generators was presented to get a better understanding about the predicting process.

II. DATA SETUP FOR DEEP LEARNING

When applying deep learning, it is important to prepare plenty of good quality data, because this primarily determines the level of predictions. Therefore, the methodologies for preparing the dataset are discussed in detail in this section.

In Fig. 1(a), an overview of the deep learning architecture proposed is presented with data flow pipelines (dark blue arrows). As shown, three types of data exist (two-channel input of laser processing parameters, weld bead segmentation, and the OM image) and two different generators (G_1 and G_2). In the first generator G_1, which was

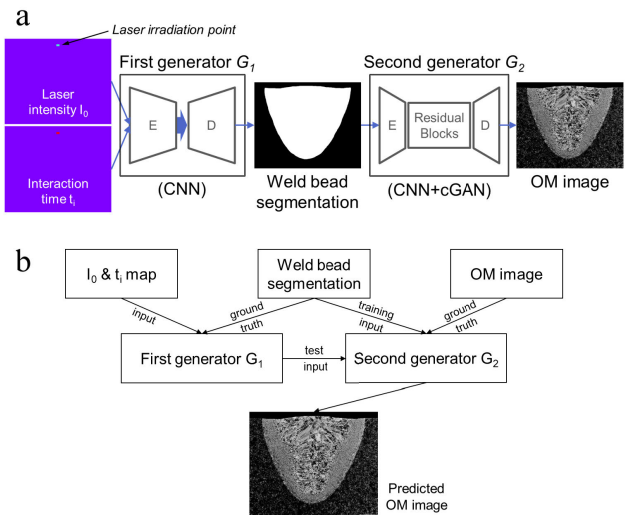

FIGURE 1. (a) Overview of the deep learning model proposed in this study. The OM image shown is that of 1800 W and 5.313 mm/s. (b) Data flowchart for the proposed deep learning model.

the CNN-based encoder (E) and decoder (D), the weld bead segmentation map was predicted from the two-channel input of the laser processing parameters (I_0 and t_i). Subsequently, in the second generator G_2, which was the CNN-based cGAN structure, the OM image was constructed from the weld bead segmentation map. A comprehensive data flowchart is given in Fig. 1(b). Note that all the figures in this article were edited using PowerPoint and Origin.

For the data setup, 45 laser welding experiments were initially conducted on a large process window (see Fig. 3), according to 45 laser process conditions (I_0, t_i). It should be noted that $I_0 = P/A_{beam}$ and $t_i = D_{beam}/v$, where P, A_{beam}, D_{beam}, and v are the laser power, laser beam area, beam diameter, and laser scanning speed, respectively. After the experiments, a cross-sectional weld bead was observed using optical microscopy; hence, 45 pairs of [(I_0, t_i), OM image] were obtained. Details regarding the experiment are presented in Section II-A.

Next, the laser processing parameters were converted into a two-channel image tensor, as shown in the leftmost of Fig. 1(a) (each channel corresponds to the I_0 map and t_i map). Furthermore, from the OM images, the weld bead segmentation maps were constructed manually, such that the pixel value inside the bead was 1.0, and 0.0 elsewhere, as shown in Fig. 1(a). Therefore, 45 pairs of [(I_0, t_i), SEG, OM image] are now ready (SEG denotes the weld bead segmentation map). Details are described in Section II-B.

Subsequently, the entire data was divided into training, validation, and test sets. To increase the number of training data, the training set was augmented by adopting several image-processing techniques that are primarily used in computer vision [29]. The details are explained in Section II-B. The detailed architectures of G_1 and G_2 are presented in Section III.

A. LASER WELDING EXPERIMENT

To obtain the OM images of the cross-sectional laser weld bead according to the laser process condition (I_0, t_i), a laser welding experiment was conducted. For the laser, a 2 KW multi-mode fiber laser (IPG YLS-2000) with a wavelength of 1070 nm was used. The laser beam exhibited a circular top-hat intensity profile, and the beam passing through a 200 μm process fiber, 160 mm collimation lens, and 160 mm focusing lens was focused on the surface of the specimen, with a focused diameter of 200 μm. In Fig. 2, a schematic drawing of the experiment is shown with coordinates and dimensions.

The specimen was a 30 mm × 40 mm × 12 mm AISI 1020 carbon steel block and its chemical composition is presented in Table 1. The specimen surface to be welded (x-y plane in Fig. 2) was grinded to a roughness of 1 μm and washed with acetone before welding, to remove impurities and cutting fluid remaining on the surface that could affect the beam penetration and surface reflection. During the experiment, the laser head was fixed and the specimen moved in the $-x$ direction on a motorized linear stage.

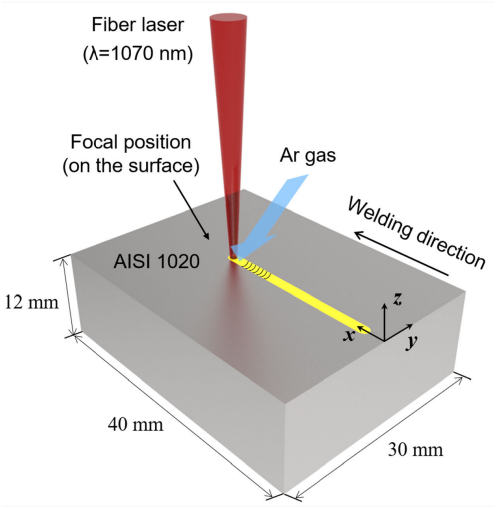

FIGURE 2. Schematics of the laser welding experiment.

TABLE 1. Chemical composition of AISI 1020 carbon steel (Mill sheet).

AISI 1020	C	Si	Mn	P	S	Fe
(%)	0.185	0.242	0.558	0.0154	0.0051	balance

Furthermore, as shown in Fig. 2, welding was performed on a bead-on-plate mode, and 25 lpm of argon gas was supplied for shielding. The shielding nozzle was a copper tube with an outer diameter of 10 mm and an inner diameter of 6 mm, and was located with a distance of 1 mm from the specimen surface (z direction in Fig. 2) and 1 mm from the laser beam position (x direction in Fig. 2). The flow angle was 45°.

Fig. 3 shows a process window showing the laser welding conditions on a laser power-scanning speed plane, and as seen, a total of 45 experiments were conducted. Laser power and beam scanning speed were ranged from 112.5 to 1800 W and from 5.313 to 340 mm/s, respectively, on a logarithmic scale. The two process conditions in a dashed square box

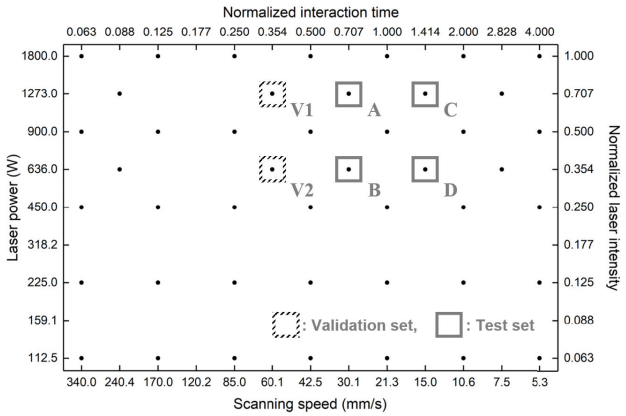

FIGURE 3. Process conditions on a laser power-scanning speed (normalized laser intensity-normalized interaction time) map.

(marked by V1 and V2) were used for the validation of the deep learning model, and those in a solid square box (marked by A, B, C, and D) were used for the test of the final model (four conditions). The process conditions without any box were applied for the training of the model (39 conditions).

After the experiments, the specimens were cut in the middle ($x = 20$ mm in Fig. 2) by electric discharge machining (EDM), and the cross-sectional weld bead was observed by optical microscopy (Axiozoom by Zeiss) after polishing and etching.

B. DATA PREPROCESSING

In this section, the details of data preprocessing are discussed. In Fig. 4, an example of a two-channel input is presented (process condition: 1800 W and 5.313 mm/s). As shown in the figure, each channel comprises 138 × 142 pixels and the laser irradiation points are magnified on the right.

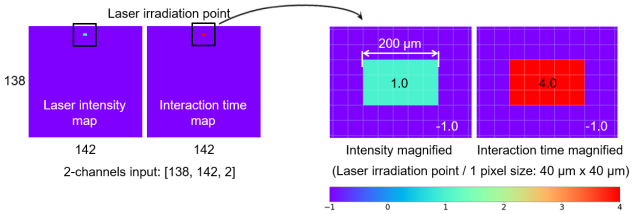

FIGURE 4. Two-channel input consisting of laser intensity and interaction time maps (size: (H = 138, W = 142, C = 2)). Laser irradiation points in laser intensity and interaction time maps are magnified on the right. Shown process condition was 1800 W and 5.313 mm/s.

As presented in the magnified images, normalized I_0 and t_i values (1.0 and 4.0, respectively) were assigned at the laser irradiation point. The normalizations were calculated by I_0/I_0^* and t_i/t_i^*, respectively (I_0^* and t_i^* were respectively calculated with respect to P = 1800 W and v = 21.25 mm/s). Thus, the normalized intensities were 0.0625, 0.125, . . . , 1.0, and the normalized interaction times were 0.0625, 0.0884, . . . , 4.0, as shown in Fig. 3. The normalized process condition was inserted at the laser irradiation point, which was a rectangle with 3 × 5 pixels (1-pixel size = 40 μm; 5 pixels in width = 200 μm = D_{beam}), and −1.0 was assigned at the other pixels. The number of pixels in height (three pixels) was determined by trial and error, near the filter size (four pixels). The location of the laser irradiation point was identified from a vertical centerline of the weld bead and the height of the material, from the OM image. The two-channel image tensor of shape (H = 138, W = 142, C = 2) was input to the first generator (H, W, and C denote the number of pixels in height, width, and channel directions, respectively).

To construct a robust AI model with a good prediction capability, the [(I_0, t_i), SEG] pairs in the training set for the first generator were augmented by adopting three different imaging techniques: flip left and right (×2), image transformation (×50), and horizontal translation (×11). Therefore, for each training process condition, ×1100 augmentation was performed; as such, the total number of [(I_0, t_i), SEG] pairs in the training set for G_1 was 42900 (39 × 1100). Similarly, the [SEG, OM image] pairs in the training set for the second generator were augmented by flip left and right (×2) and horizontal translation (×21); therefore, the total number of training data pairs was 1638 (39 × 42). Note that the AI model must be trained with a large amount of data to cope with various situations, and thus proper data augmentation is essential for a successful learning. For instance, in laser keyhole welding, the keyhole interface fluctuates by high interfacial forces such as capillary and thermocapillary forces and recoil pressure [5], [6], so the bead shape is not always constant but varies a bit. Therefore, for the AI model to learn about the slightly different bead shapes caused from the multi-physics phenomena, the weld bead segmentation maps (ground truth) in the first generator were augmented by applying a random weak shear transformation. Meanwhile, corresponding inputs of I_0 and t_i maps were not transformed because the AI model had to learn that slightly changing bead shapes could occur from the same laser process condition.

III. PROPOSED DEEP-LEARNING MODEL

The deep learning model proposed in this study is composed of two training sessions of the first and second generators (G_1 and G_2). In the first generator, the two-channel input was translated into a weld bead segmentation map, through the CNN-based encoder–decoder network. Through the encoding line, the training filters in the CNN extract essential information contained in the input image according to the given loss function, and through the decoding line, the filters reconstruct the encoded features to the desired image. In the second generator, the weld bead segmentation map was input, and the generator learned to fill the map into an OM image, through the CNN-based cGAN network (pix2pixHD). Both deep learning models were implemented using Python™ and the TensorFlow™ library, on a i7-7820X CPU and dual GTX 1080 Ti GPUs.

A. THE FIRST GENERATOR

A flow diagram and the structure of the first generator are presented in Fig. 5(a) and Fig. 5(b), respectively. As shown, the two-channel input and weld bead segmentation ground truth were denoted by c and x, respectively, and the predicted (generated) segmentation map from the generator was $G_1(c)$.

In Fig. 5(a), an overall flow for the first generator is shown with a loss and an optimizer. As shown, the first generator is composed of an encoder and decoder (denoted by E and D in the figure, respectively). Mathematically, it was defined as

$$G_1 = G_1(c; \theta^{G_1}), \tag{1}$$

where θ^{G_1} are the training variables in G_1, i.e., weights and biases in the convolutional processes, which are filters W and bias b in Fig. 6. θ^{G_1} was trained to translate the two-channel input to a bead segmentation map, according to the following mean absolute error loss function J^{G_1} (mean of

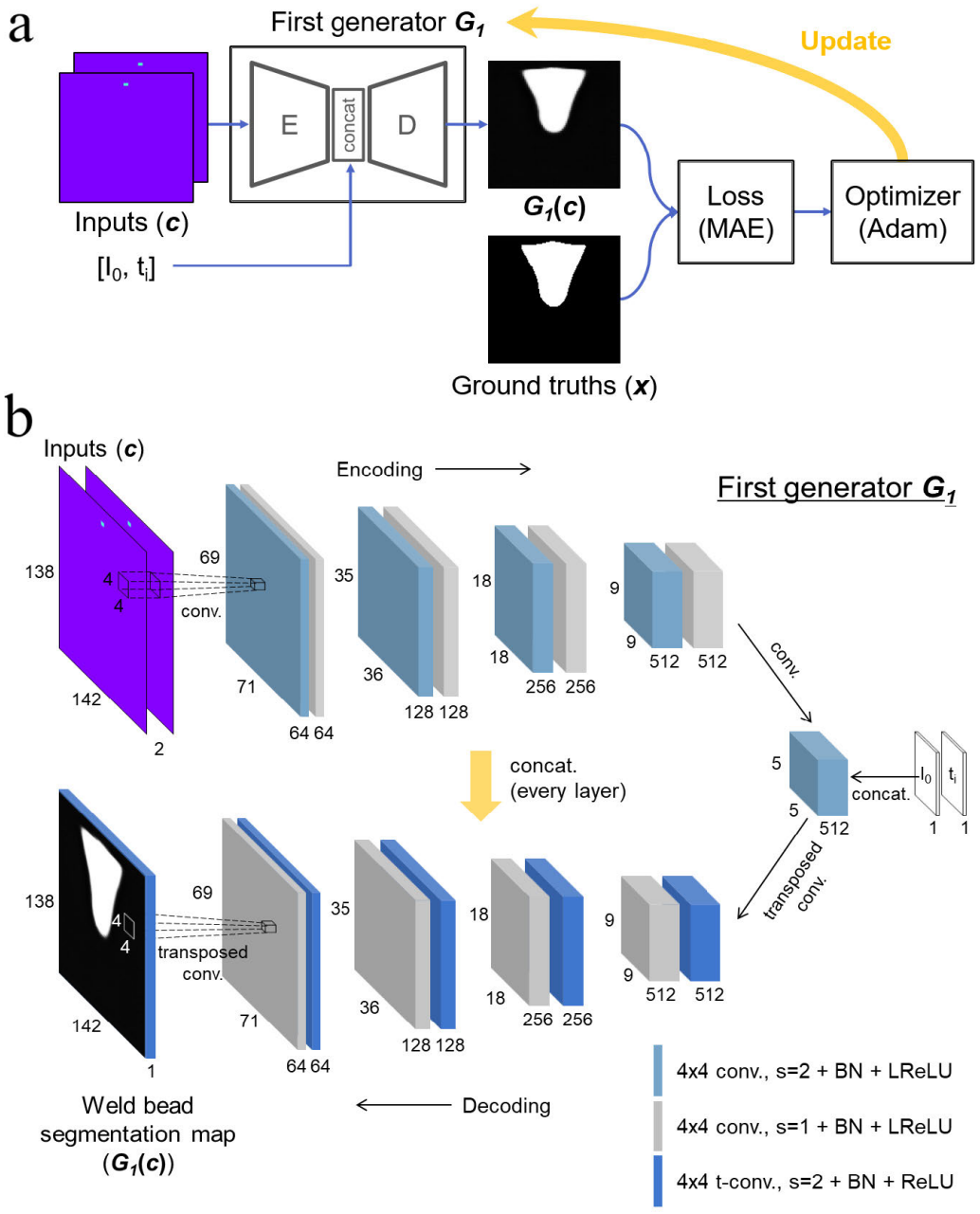

FIGURE 5. (a) Flow diagram for training the first generator. Shown process condition was 1800 W and 21.25 mm/s. (b) Detailed structure of the first generator. It consists of successive convolution-BN-activation layers.

absolute difference between the ground truths and the generated segmentation images) [30]:

$$J^{G_1}(\theta^{G_1}) = \frac{1}{HW} \sum_{i=1}^{H=138} \sum_{j=1}^{W=142} |x - G_1(c)|. \quad (2)$$

The optimizer subsequently updates θ^{G_1} toward minimizing the given loss function by backpropagation, i.e., to decrease the difference between the ground truths and the predictions. Note that a mean squared error loss function was also tested but could not get a better result. For the optimizer, an adaptive moment estimation (Adam) proposed by Kingma and Ba [31] was used.

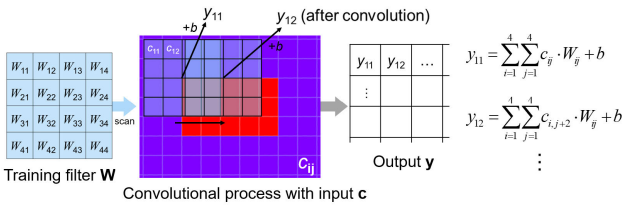

FIGURE 6. Schematic diagram for the convolution. 4 × 4 training filter W scanned the input c with stride 2, and output y. The filter and the 4 × 4 patches of the input were multiplied element wise, and subsequently summed.

In Fig. 5(b), three different colored operation-blocks are shown inside G_1. In each block, the (H, W, C) numbers are

written in a counter-clockwise direction, starting from the vertical edge. The light blue block consisted of 4 × 4 convolution (conv.) (strides = 2)–batch normalization (BN)–leaky rectified linear unit (LReLU; max$(0.2x, x)$) [32] layers. Fig. 6 shows a schematic of the convolutional process [18] between the input image **c** and training filter **W**. In the figure, a 4 × 4 filter **W** scans the input image **c** with stride 2. First, the filter is element-wise multiplied to the first 4 × 4 patch of the input (the 4 × 4 square, which contains c_{11}, c_{12}) and subsequently summed together with the bias b, thus resulting in an output y_{11} (the first pixel of the output image **y**). This process is successively conducted on the entire input image (channel by channel), and the output image **y** now exhibits smaller dimensions in H and W compared to the input (encoded). In the CNN, this convolutional process is repeated through several layers, and as the network deepens, higher levels of features included in the input image are extracted [33], [34].

After convolution, batch normalization was performed such that the input batch exhibits a zero mean and unity standard deviation in each channel. Ioffe and Szegedy [35] first used this layer, for the gradients in backpropagation not to vanish or explode. In addition, using this layer, overfitting to the training set is suppressed, the learning speed improves, and the dependency to the initial distributions of the training variables decreases. After batch normalization, a nonlinear activation layer was added (LReLU in light blue and gray blocks, and ReLU in dark blue block).

The gray block represents operations of 4 × 4 convolution with stride 1–BN–LReLU, and the dark blue block represents a 4 × 4 transposed-convolution [36] with stride 2–BN–rectified linear unit (ReLU; max(0, x)) [37]. In Fig. 5(b), the transposed-convolution was denoted by "t-conv." This restores the dimensionality of the encoded features, by applying trainable filters to the input. The calculation of t-conv. is the reverse of the convolutional process, i.e., a 4 × 4 filter is element-wise multiplied to each broadcasted pixel in the input, and subsequently summed with the bias. The output exhibits higher dimensions in H and W (decoded). It is noteworthy that the last dark blue block represent operations of 4 × 4 transposed-convolution with stride 2–tanh, without BN.

As shown in Fig. 5(b), in the encoding line (top row), the two-channel input of the laser processing parameters was encoded to smaller dimensions through series of convolutional layers; additionally, through the decoding line (bottom row), the encoded bottleneck (H = 5, W = 5, C = 514) was upsampled to achieve input-level resolution (H = 138, W = 142, C = 1).

Additionally, skip connections between the encoder and decoder were used (orange vertical arrow in Fig. 5(b)), which were concatenation processes in each layer's channel direction. Ronneberger *et al.* [38] first proposed this structure to provide encoded features to the decoding line, which resulted in a much better quality of the synthesized images. In the bottleneck layer, the two laser processing parameters of I_0 and t_i were broadcasted and concatenated in the channel direction, as shown in both Fig. 5(a) and Fig. 5(b), to directly provide information about the process condition to the upsampling line. The concatenations were denoted by "concat." in the figure.

B. THE SECOND GENERATOR

After the first generator was trained, the second generator was trained with the weld bead segmentation map as an input and the OM image as a ground truth, as presented in Fig. 1, Fig. 7(a), and Fig. 7(b). Both were (H = 552, W = 568, C = 1) in size, and in the case of such a high-resolution image generation problem, unstable generations have been a critical problem. For instance, when applying pix2pix [39] to our second generator, many repeated patterns were observed in the generated images. Hence, in this study, pix2pixHD [19] was employed in the second generator, which demonstrated particularly good results in a high-resolution image-to-image translation problem. Its primary framework is a CNN-based cGAN, with multi-scale generators and discriminators, and deep residual networks.

In Fig. 7(a), a data flow diagram is shown, with the second generator, multiscale discriminators, loss, and Adam optimizer. The input weld bead segmentation map is denoted by y, which was the result of the first generator ($G_1(c)$ in the validation and the test phases) or SEG (x, in the training phase). It is noteworthy that in the case of $G_1(c)$ as an input, it was 4× upsampled using bilinear interpolation before input to the second generator ((138, 142, 1)→(552, 568, 1)). The ground truth OM image was denoted by OM. Subsequently, the input y was translated to the OM image through the second generator, which was trained according to the loss functions given by the multiscale discriminators. The multiscale discriminators (D_k) operated in three different scales: D_1 at an original size, and D_2 and D_3 respectively at 2× and 4× downsampled sizes. According to pix2pixHD, to correctly distinguish between real and fake from high-resolution images, the discriminator must have a large receptive field (extremely deep layers or large convolutional filters); however, the training data would be overfitted and a larger memory would be required. Instead, they adopted multiscale discriminators while fixing the number of layers and the filter size (all the discriminators share the same network structure).

Mathematically, the second generator and the discriminator are expressed as

$$\begin{aligned} G_2(y) &= (G_{global}(y'), G_{local}(y)), \\ D_k &= D_k([G_2(y)\ or\ OM]|\, y). \end{aligned} \tag{3}$$

As written, the second generator is a tuple of a global generator network (G_{global}, middle encoder-9 residual blocks-decoder network in Fig. 7(b)) and a local enhancer network (G_{local}, the remaining network excluding G_{global}, in Fig. 7(b)). Both networks were of an encoder-residual blocks-decoder structure but operated at different scales, i.e., G_{global} at a 2× downsampled scale (H = 276, W = 284)

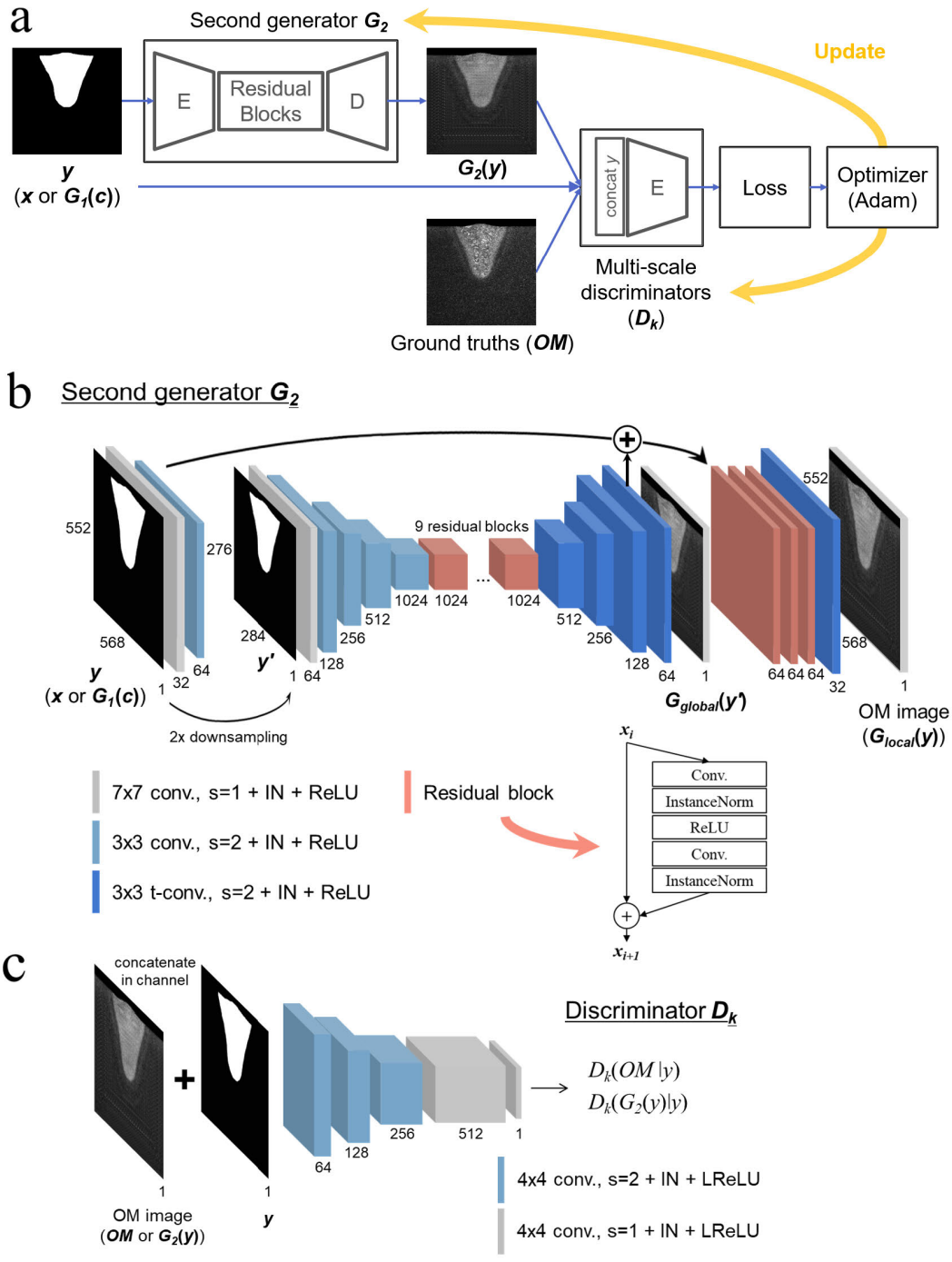

FIGURE 7. (a) cGAN flow diagram for training the second generator and multiscale discriminators. Shown process condition was 1800 W and 21.25 mm/s. (b) Detailed structure of the second generator with the residual block configuration. (c) Detailed structure of the discriminator. Multiscale discriminators share the same operations.

and G_{local} at the full scale (H = 552, W = 568). y' denotes the 2× downsampled y, which was the input to the global generator. The vertical bar y represents the concatenation process in the channel direction between the weld bead image and y. For the loss function, based on the traditional GAN loss (J_{GAN}) that was given by (𝔼: expectation)

$$J_{GAN}(G_2, D_k) = \mathbb{E}_{OM,y}[\log D_k(OM|y)] + \mathbb{E}_y[\log(1 - D_k(G_2(y)|y))], \quad (4)$$

the full objective function was constructed with a feature matching loss (J_{FM}), as depicted in pix2pixHD:

$$\min_{G_2}\left(\left(\max_{D_1,D_2,D_3}\sum_{k=1,2,3} J_{GAN}(G_2, D_k)\right) + \lambda \sum_{k=1,2,3} J_{FM}(G_2, D_k)\right). \quad (5)$$

Mathematical details regarding the GAN loss and feature-matching loss can be found in ([19]–[21], [40]) and are omitted here for brevity. By maximizing the given loss term ($D_k(OM|y) \rightarrow 1$ and $D_k(G_2|y) \rightarrow 0$), the multiscale discriminators are trained to correctly distinguish the real input (OM) and the generated input ($G_2(y)$ i.e., $G_{global}(y')$ or $G_{local}(y)$). Meanwhile, the generator is trained to create more realistic images, to fool the discriminator by minimizing the given loss term ($D_k(G_2|y) \rightarrow 1$ and feature-matching loss).

In Fig. 7(b), the network structure of the second generator is presented; it consists of the global generator (CNN-based encoder–9 residual blocks–decoder) and the local enhancer (the rest). The gray, light blue, and dark blue blocks are operations of 7×7 convolution with stride 1–instance normalization (IN) [41]–ReLU, 3×3 convolution with stride 2–IN–ReLU, and 3×3 transposed-convolution with stride 2–IN–ReLU (the last gray block in the decoders are operations of 7×7 convolution with stride 1–tanh), respectively. The local enhancer network receives the last 64-channel feature map in the global generator (element-wise summation with the same-shaped encoded feature map) and raises its resolution through the following three residual blocks–decoder network. Training was performed in the order of global generator, local enhancer, and both. The configuration of the residual blocks [23] is shown in the figure. It is noteworthy that other well-known residual structures such as ResNet [22], full pre-activation [42], and EDSR [25] were tested, but did not achieve significantly better results. In addition, to reduce the computational cost, several simplified models were tested, such as removing the local enhancer (only global generator), decreasing the number of residual blocks, using only two discriminators, and utilizing skip connections [38] between the encoder and decoder; however, acceptable qualities could not be obtained.

In Fig. 7(c), the discriminator structure is shown. It is the CNN-based encoder, and the light blue and gray blocks are operations of 4×4 convolution with stride 2–IN–LReLU and 4×4 convolution with strides 1–IN–LReLU, respectively. In both Fig. 7(b) and Fig. 7(c), the number of channels in each operation is written under the block.

C. TRAINING INFORMATION

For the first generator, the learning rate, batch size, and exponential decay rate for the first moment estimate in the Adam optimizer (β_1) were 10^{-7}, 100, and 0.9, respectively. For the second generator, they were 0.0002 (linearly decaying to 1/100 from 0.0002 for every 100 epoch), 1, and 0.5, respectively. All the weights were initialized to a Gaussian distribution with a mean of 0.0 and a standard deviation of 0.02 [43], and all the bias to 0.0, in both G_1 and G_2. All the downsamplings were conducted by average pooling. The root mean square errors (RMSEs) of the first generator for the training and validation sets are given in Fig. 8 according to the number of epochs.

As shown in the figure, the validation error continued increasing after reaching the minimum at epoch 295, so the training was stopped there. In the second generator, training was conducted as long as possible considering the computing time, and was stopped at epoch 160.

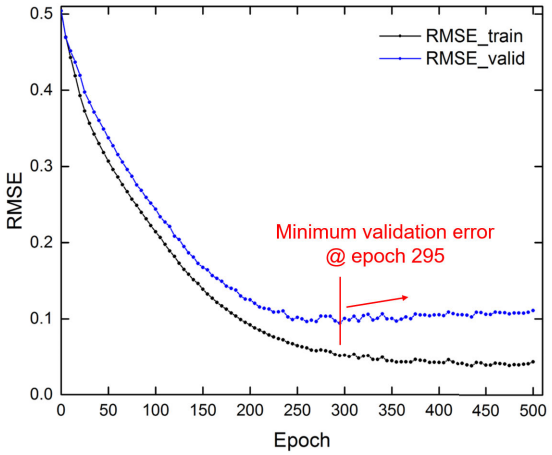

FIGURE 8. Training and validation RMSE curves of the first generator according to the number of epochs.

IV. RESULTS AND DISCUSSION

The prediction results for the test dataset are presented in Fig. 9. In each row from top to bottom, the process conditions were A, B, C, and D (see Fig. 3). In the first two columns, inputs (c) to the deep-learning model (laser intensity map and interaction time map) are shown separately, with the normalized processing parameters (numbers inside the parenthesis are the corresponding laser powers or scanning speeds). In the third column, the prediction results of the weld bead segmentation ($G_1(c)$; output of the first generator at epoch 295) are drawn and the corresponding ground truths (x) are given in the fourth column. In the fifth column, final predictions of the OM image ($G_{local}(G_1(c))$; output of the local enhancer network when the epoch was 160) are presented, and their ground truths (OM) are given in the final column. It is noteworthy that in the test phase, the input to the second generator was the first generator's results ($G_1(c) \rightarrow y$), as explained previously.

As shown in Fig. 9, the AI model created the weld bead images that is quite similar to the actual cases, in terms of bead shape and penetration depth. To evaluate the performance of the model, the penetration depth and weld bead area of the prediction result and ground truth for four test process conditions (A, B, C, and D) were measured, and shown in Fig. 10. All the data of penetration depth and bead area in the figure were normalized with respect to the maximum penetration depth and maximum bead area, respectively. The y-axis and x-axis were prediction result and ground truth, respectively, and the penetration depth was marked by circle and the weld bead area by star. As shown in the figure, the data distribution appears to be close to the $y = x$ line (prediction $\approx$ ground truth) and calculated R-Squared accuracy was 89.0% for penetration depth and 93.6% for weld bead area. In terms of the R-Squared accuracies and overall aspect of the weld

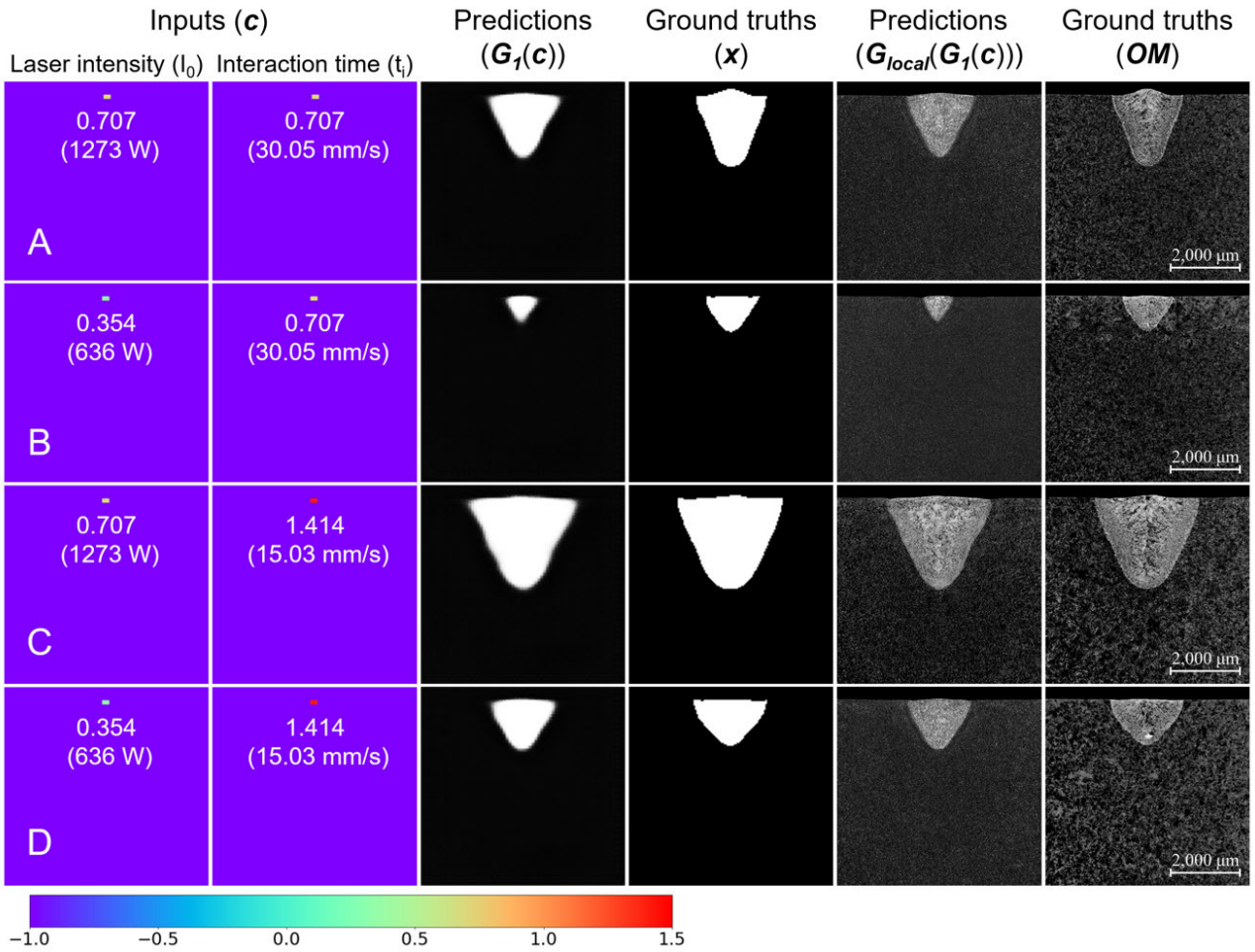

FIGURE 9. Test set results (from top to bottom, A, B, C, D). The first and the second columns are input normalized laser intensity and interaction time maps (*c*), respectively. The third and the fourth columns are prediction results for the first generator ($G_1(c)$) and their ground truths (x), respectively. In the fifth and the sixth columns, predicted OM images ($G_{local}(G_1(c))$) and ground truths (OM) are presented, respectively.

bead in Fig. 9, it can be concluded that the AI model predicted the weld beads fairly well, from the laser processing parameters.

Fig. 11 presents predicted and ground truth OM images of the process condition C that demonstrated the largest bead size and the highest bead shape accuracy (see Fig. 10; closest to the $y = x$ line). Even though the predicted grain details were substantially different compared to the ground truth, the shape and size of the overall weld bead were well predicted, and the molten zone near the bead boundary was fairly well distinguished from the central region. Furthermore, despite the high resolution of the image, the generated images were clear without any unstable or repeated regions, owing to the multi-scale generators and discriminators, and deep residual networks adopted in the second generator, as utilized in ([24]–[28]).

In Fig. 12 and Fig. 13, the insides of the two generators were open to track the predicting process when the process condition of 1800 W, 5.313 mm/s (training set; Fig. 12) and 1273 W, 15.03 mm/s (test set, C; Fig. 13) were input. The

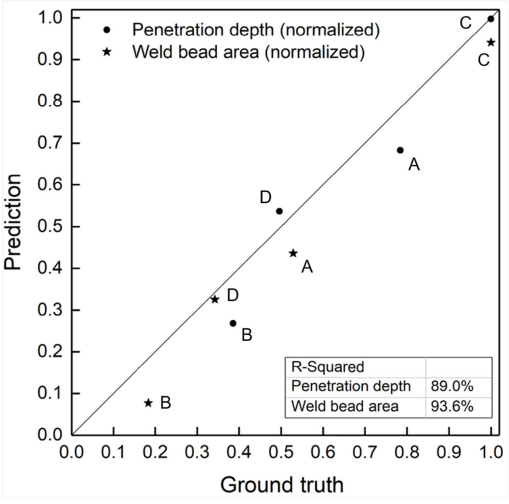

FIGURE 10. Graphical comparison between the prediction result (y-axis) and the ground truth (x-axis) for four test process conditions (A, B, C, D), in terms of penetration depth (marked by circle) and weld bead area (marked by star). All the values were normalized with respect to the maximums. Corresponding R-Squared accuracies are written in the bottom-right corner.

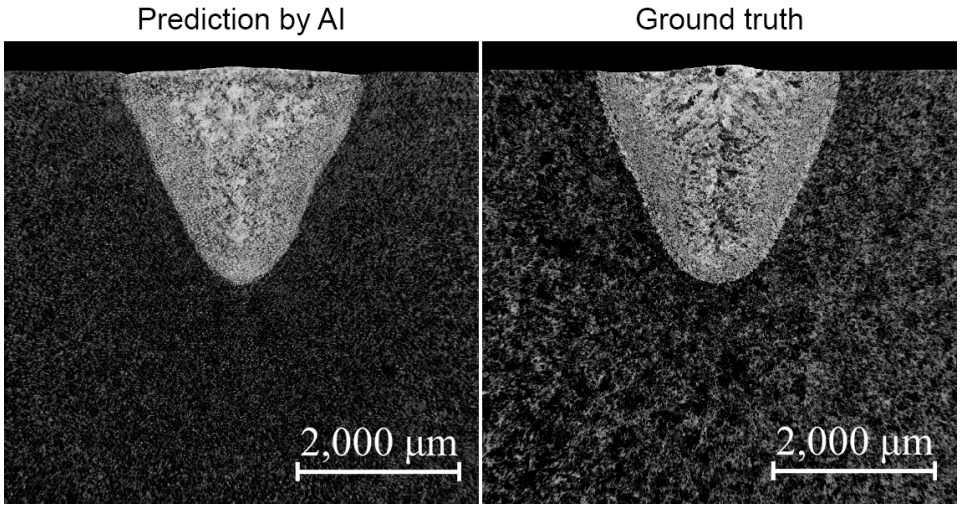

FIGURE 11. (Left) High-resolution (H = 552, W = 568, C = 1) OM image predicted by AI. (Right) Ground truth image. The laser process conditions were 1273 W and 15.03 mm/s (C).

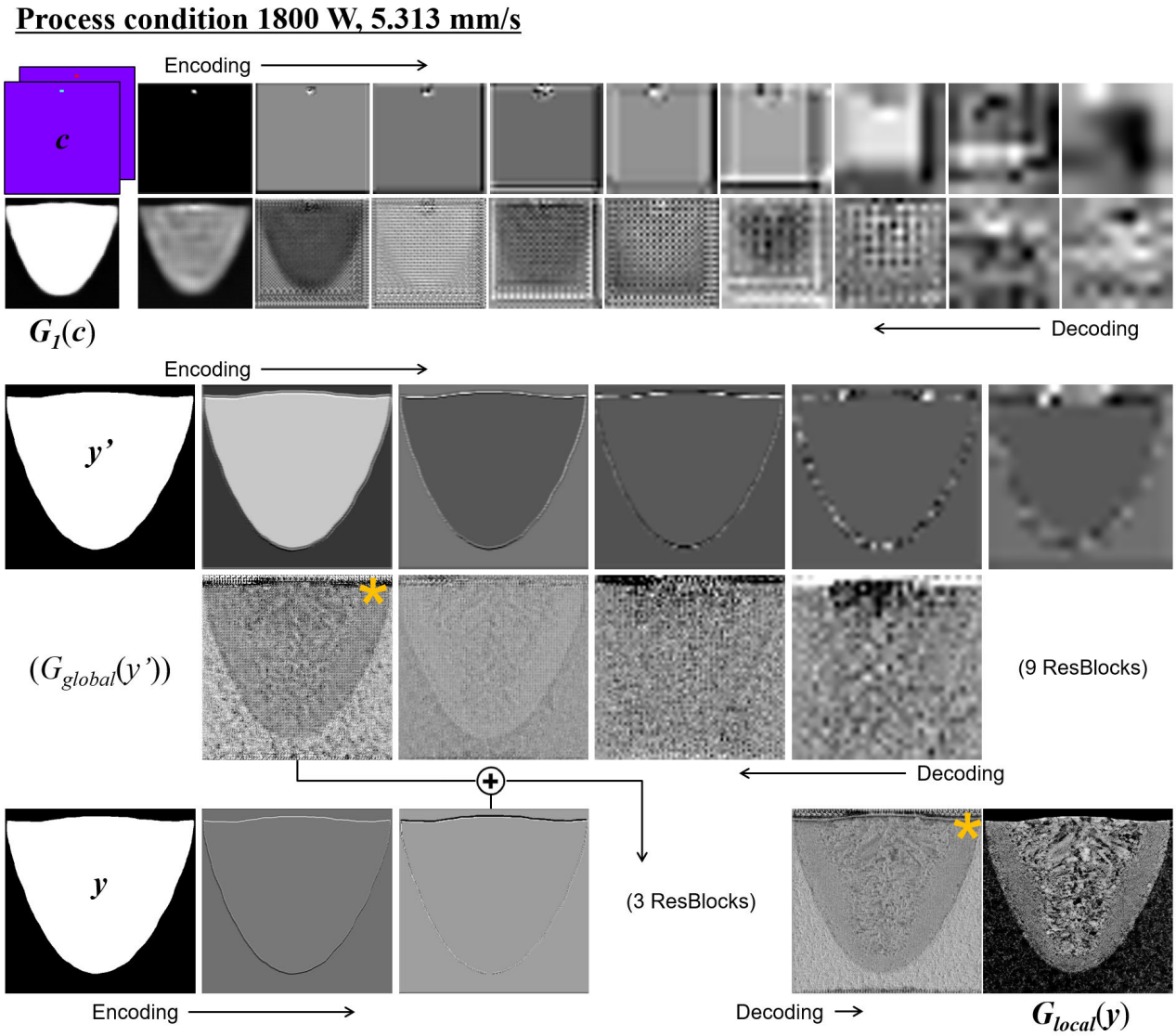

FIGURE 12. Insides of the two generators when the process condition of 1800 W and 5.313 mm/s was input (training set). Upper two rows are the first generator and lower three rows are the second generator. In the second generator, global generator (upper two rows) and local enhancer (last row) are shown with data pipelines.

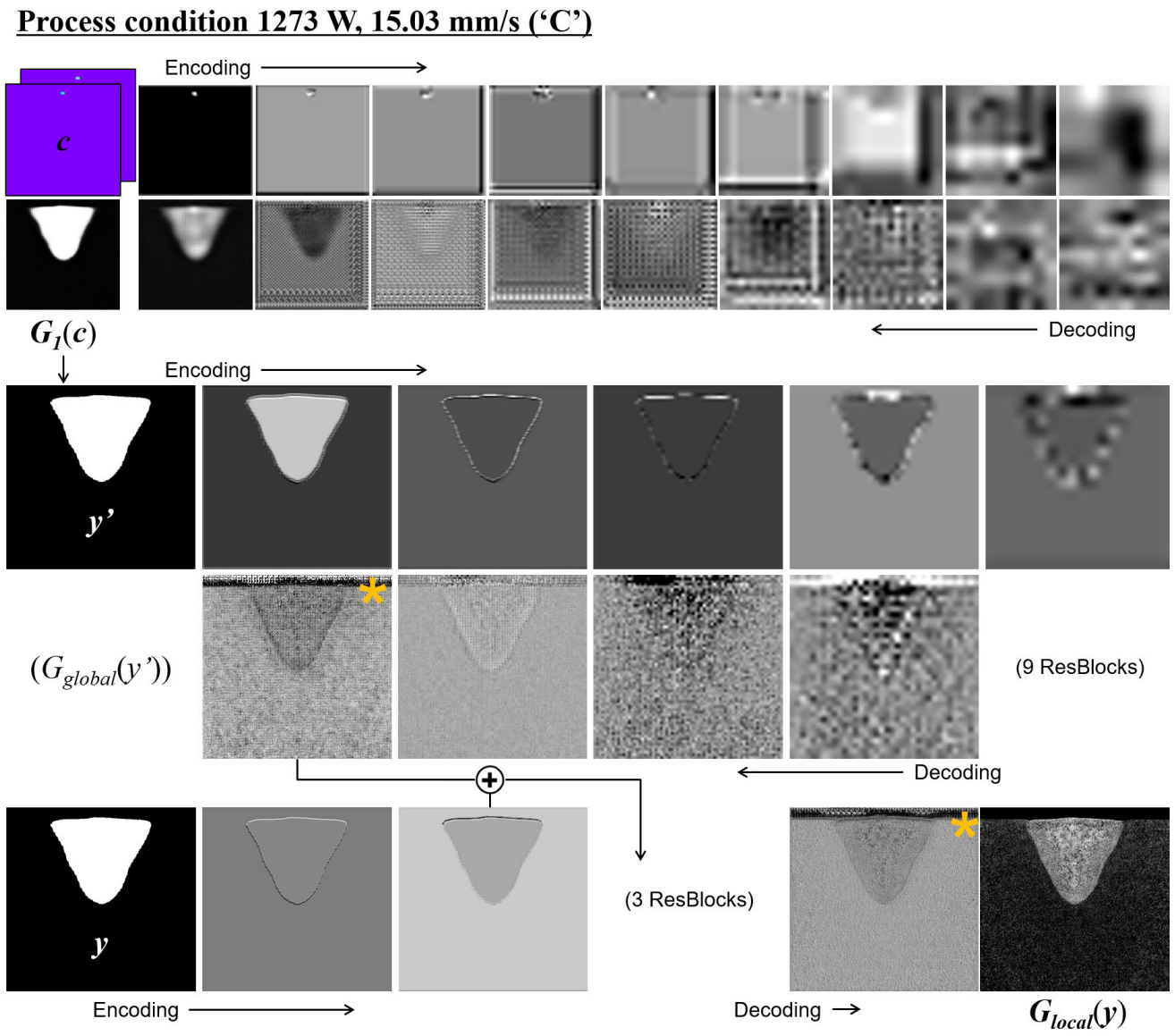

FIGURE 13. Insides of the two generators when the process conditions of 1273 W and 15.03 mm/s was input (test set, C). Upper two rows are the first generator and lower three rows are the second generator. In the second generator, global generator (upper two rows) and local enhancer (last row) are shown with data pipelines.

top two rows are the first generator at epoch 295 and the bottom three rows are the second generator at epoch 160. Only the first channel (C = 1) was shown for brevity. In the first generator, the encodings of the input progressed along the top line from left to right and the decodings were conducted in the bottom line from right to left. In the second generator, the global generator was presented in the upper two rows (encodings in the first row and decodings in the second row), and the local enhancer was in the last bottom row. As presented, the local enhancer accepts the lower resolution feature maps from the global generator and increases the resolution to the full scale, as clearly shown by comparing two starred feature maps, which were the closest layers to each end. It is worth noting here that in this way, by adding extra enhancers operating at larger scales, it is possible to generate even higher resolution bead images [19] (H = 552, W = 568 → H = 1104, W = 1136 → …; although it will require more and more GPU cost), which can help actualize the microstructures.

Fig. 14 presents the extracted feature maps of the closest layer to the end of the local enhancer. The process conditions were 1800 W and 5.313 mm/s (training set) in the left figure, and 1273 W and 15.03 mm/s (test set, C) in the right figure. (They are the magnified second starred image in Fig. 12 and the image at the same layer in Fig. 13, respectively). As shown, the heat affected zones (marked by yellow arrows in the figure) of the test set were fairly well recognized, as in the training set case. Meanwhile, the grain details inside the beads were realized but not correctly, as discussed in Fig. 11. This remains as future work.

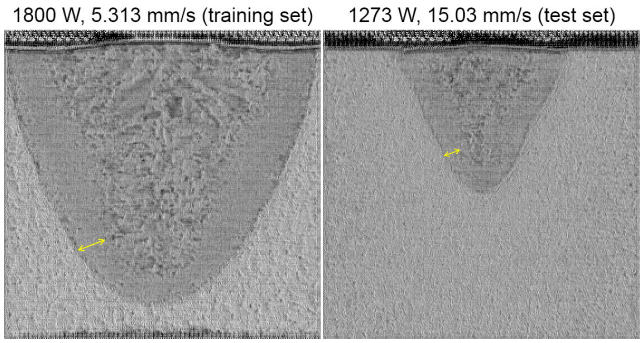

FIGURE 14. Feature map comparison between the training set (1800 W and 5.313 mm/s, left figure) and test set (1273 W and 15.03 mm/s, right figure). The feature maps were extracted from the last second layer in the local enhancer network.

Additionally, supplement of raw data must be preceded in the subsequent study, as it is the easiest way to make the deep learning model more robust and precise. For instance, with the proposed amount of data (39 training; 4 testing), the adjusted R-Squared ($R^2_{adj} = 1 - (1 - R^2)(n - 1)/(n - p - 1)$; the number of test data $n = 4$; the number of variables $p = 2$ (I_0, t_i)) of the test set was 67.0% for penetration depth and 80.9% for weld bead area. However, if slightly increasing the amount of raw data to (49 training; 5 testing), about 10% increase of R^2_{adj} is expected, as the number of test data points increases ($n = 4 \rightarrow 5$) and as the test R-Squared improves (for most cases, as the number of training data increases, so is the test accuracy assuming that the deep learning model is well trained and validated). Thus, as data accumulates, more and more robust and accurate deep learning model can be built.

Also, in the subsequent deep learning-based study, additional input variables such as an ambient pressure and shielding condition can be introduced to the first generator, as they largely affect the weld bead [44]–[47]. It will be also worth studying about the keyhole fluctuation effect, which leads to the fluctuating bead shapes under the same laser process condition. Our results showed that the data augmentation methods adopted in this study worked fine, however, a more fundamental study on this subject may be conducted in the future.

Lastly, interactions between the input variables on the bead shape can be identified by statistically investigating the convolutional weights after training, as it can contribute to the establishment of a simplified predictive model. It did not proceed in this study as it was beyond the scope of this paper, but it could be simply checked from the raw data, to investigate the influence and interaction of the variables. When tested with a two-way analysis of variance (ANOVA) using MATLAB (for 35 process conditions on a larger uniform grid in Fig. 3), it was statistically confirmed that both of I_0 and t_i have a significant effect on the penetration depth, as presented in Table 2 (p-values $= 1.05 \times 10^{-6}$, 0.00392). The effect of interaction term ($I_0 t_i$) could not be identified here, as a replication number of the experiments was one. But when tested with a general regressive model ($Y = a + bI_0 + ct_i + dI_0 t_i$ where a, b, c, d are constants, $I_0 t_i$ is an interaction term, I_0 and t_i were normalized to the maximums, and Y is the penetration depth; fitting method was a nonlinear least squares in MATLAB), the constants a, b, c, and d were -0.09624, 1.441, -0.06814, and 4.146, respectively (R-Squared: 90.3%). It indicates that I_0 and t_i do interact on the penetration depth, i.e. the effect of laser intensity on the penetration depth depends on interaction time, and vice versa. Note that our deep learning model could learn this nature spontaneously, by observing the given training data.

TABLE 2. Analysis of variance (ANOVA) table for the penetration depth (conducted in MATLAB). (SS, df, and MS denote summation of squares, degrees of freedom, and mean squares, respectively. α was 0.05.)

Source	SS	df	MS	F	p-value	F_{cri}
I_0	25.401	4	6.350	16.86	1.05E-6	2.78
t_i	9.930	6	1.655	4.4	0.00392	2.51
Error	9.037	24	0.377			
Total	44.368	34				

V. CONCLUSION

A novel framework of predicting cross-sectional laser weld bead images was presented, using state-of-the-art deep learning architectures. The first generator could predict the bead segmentation map (i.e. weld bead shape) from the two laser processing parameters of laser intensity and interaction time, and the second generator could fill the segmentation map into the optical microscopic bead image. Trained from only 39 pairs of raw data (39 laser process conditions), the generators predicted the laser weld bead with R-Squared accuracies of 89.0% for penetration depth and 93.6% for weld bead area, and the generated bead images were of high resolution without partial repetitions or distortions. Also, heat affected zone inside the bead was well distinguished from the keyhole area.

However, grain details inside the weld bead were not fully actualized, and the resolution of the generated bead image was less than that of the actual microscopic images (generally 500∼2000 pixels on each side). Thus, future work includes scaling-up of the generated images in both generators which also can help realize the grain details (e.g. by stacking additional enhancer networks), and the issues of raw data increment and input variable analysis as discussed in the previous section.

REFERENCES

[1] A. Squillace, U. Prisco, S. Ciliberto, and A. Astarita, "Effect of welding parameters on morphology and mechanical properties of Ti–6Al–4 V laser beam welded butt joints," *J. Mater. Process. Technol.*, vol. 212, no. 2, pp. 427–436, Feb. 2012, doi: 10.1016/j.jmatprotec.2011.10.005.

[2] K. N. Lankalapalli, J. F. Tu, and M. Gartner, "A model for estimating penetration depth of laser welding processes," *J. Phys. D, Appl. Phys.*, vol. 29, no. 7, pp. 1831–1841, Jul. 1996, doi: 10.1088/0022-3727/29/7/018.

[3] C. Lampa, A. F. H. Kaplan, J. Powell, and C. Magnusson, "An analytical thermodynamic model of laser welding," *J. Phys. D: Appl. Phys.*, vol. 30, no. 9, pp. 1293–1299, May 1997, doi: 10.1088/0022-3727/30/9/004.

[4] W. S. Chang and S. J. Na, "A study on the prediction of the laser weld shape with varying heat source equations and the thermal distortion of a small structure in micro-joining," *J. Mater. Process. Technol.*, vol. 120, nos. 1–3, pp. 208–214, Jan. 2002, doi: 10.1016/S0924-0136(01)00716-6.

[5] H. Ki, J. Mazumder, and P. S. Mohanty, "Modeling of laser keyhole welding: Part I. Mathematical modeling, numerical methodology, role of recoil pressure, multiple reflections, and free surface evolution," *Metall. Mater. Trans. A*, vol. 33, no. 6, pp. 1817–1830, Jun. 2002, doi: 10.1007/s11661-002-0190-6.

[6] H. Ki, J. Mazumder, and P. S. Mohanty, "Modeling of laser keyhole welding: Part II. Simulation of keyhole evolution, velocity, temperature profile, and experimental verification," *Metall. Mater. Trans. A*, vol. 33, no. 6, pp. 1831–1842, Jun. 2002, doi: 10.1007/s11661-002-0191-5.

[7] K. Y. Benyounis, A. G. Olabi, and M. S. J. Hashmi, "Effect of laser welding parameters on the heat input and weld-bead profile," *J. Mater. Process. Technol.*, vols. 164–165, pp. 978–985, May 2005, doi: 10.1016/j.jmatprotec.2005.02.060.

[8] D. B. Hann, J. Iammi, and J. Folkes, "A simple methodology for predicting laser-weld properties from material and laser parameters," *J. Phys. D, Appl. Phys.*, vol. 44, no. 44, Nov. 2011, Art. no. 445401, doi: 10.1088/0022-3727/44/44/445401.

[9] J. Volpp and F. Vollertsen, "Analytical modeling of the keyhole including multiple reflections for analysis of the influence of different laser intensity distributions on keyhole geometry," *Phys. Procedia*, vol. 41, pp. 460–468, 2013, doi: 10.1016/j.phpro.2013.03.102.

[10] M. Courtois, M. Carin, P. L. Masson, S. Gaied, and M. Balabane, "A new approach to compute multi-reflections of laser beam in a keyhole for heat transfer and fluid flow modelling in laser welding," *J. Phys. D, Appl. Phys.*, vol. 46, no. 50, Dec. 2013, Art. no. 505305, doi: 10.1088/0022-3727/46/50/505305.

[11] J. Kim and H. Ki, "Scaling law for penetration depth in laser welding," *J. Mater. Process. Technol.*, vol. 214, no. 12, pp. 2908–2914, Dec. 2014, doi: 10.1016/j.jmatprotec.2014.06.025.

[12] W. J. Suder and S. Williams, "Power factor model for selection of welding parameters in CW laser welding," *Opt. Laser Technol.*, vol. 56, pp. 223–229, Mar. 2014, doi: 10.1016/j.optlastec.2013.08.016.

[13] R. Fabbro, "Scaling laws for the laser welding process in keyhole mode," *J. Mater. Process. Technol.*, vol. 264, pp. 346–351, Feb. 2019, doi: 10.1016/j.jmatprotec.2018.09.027.

[14] K. R. Balasubramanian, G. Buvanashekaran, and K. Sankaranarayanasamy, "Modeling of laser beam welding of stainless steel sheet butt joint using neural networks," *CIRP J. Manuf. Sci. Technol.*, vol. 3, no. 1, pp. 80–84, Jan. 2010, doi: 10.1016/j.cirpj.2010.07.001.

[15] W. S. Chang and S. J. Na, "Prediction of laser-spot-weld shape by numerical analysis and neural network," *Metall. Mater. Trans. B*, vol. 32, no. 4, pp. 723–731, Aug. 2001, doi: 10.1007/s11663-001-0126-3.

[16] L. Jacques and A. El Ouafi, "ANN based predictive modelling of weld shape and dimensions in laser welding of galvanized steel in butt joint configurations," *J. Minerals Mater. Characterization Eng.*, vol. 6, no. 3, pp. 316–332, 2018, doi: 10.4236/jmmce.2018.63022.

[17] G. E. Hinton, "Reducing the dimensionality of data with neural networks," *Science*, vol. 313, no. 5786, pp. 504–507, Jul. 2006, doi: 10.1126/science.1127647.

[18] Y. Lecun, L. Bottou, Y. Bengio, and P. Haffner, "Gradient-based learning applied to document recognition," *Proc. IEEE*, vol. 86, no. 11, pp. 2278–2324, Nov. 1998, doi: 10.1109/5.726791.

[19] T.-C. Wang, M.-Y. Liu, J.-Y. Zhu, A. Tao, J. Kautz, and B. Catanzaro, "High-resolution image synthesis and semantic manipulation with conditional GANs," in *Proc. IEEE/CVF Conf. Comput. Vis. Pattern Recognit.*, Jun. 2018, pp. 8798–8807.

[20] I. J. Goodfellow, "Generative adversarial nets," in *Proc. Adv. Neural Inf. Process. Syst.*, vol. 27, 2014, pp. 2672–2680.

[21] M. Mirza and S. Osindero, "Conditional generative adversarial nets," 2014, *arXiv:1411.1784*. [Online]. Available: http://arxiv.org/abs/1411.1784

[22] K. He, X. Zhang, S. Ren, and J. Sun, "Deep residual learning for image recognition," in *Proc. IEEE Conf. Comput. Vis. Pattern Recognit. (CVPR)*, Jun. 2016, pp. 770–778.

[23] S. Gross and M. Wilber. (2016). *Training and Investigating Residual Nets*. [Online]. Available: http://torch.ch/blog/2016/02/04/resnets.html

[24] C. Ledig, L. Theis, F. Huszar, J. Caballero, A. Cunningham, A. Acosta, A. Aitken, A. Tejani, J. Totz, Z. Wang, and W. Shi, "Photo-realistic single image super-resolution using a generative adversarial network," in *Proc. IEEE Conf. Comput. Vis. Pattern Recognit. (CVPR)*, Jul. 2017, pp. 4681–4690.

[25] B. Lim, S. Son, H. Kim, S. Nah, and K. M. Lee, "Enhanced deep residual networks for single image super-resolution," in *Proc. IEEE Conf. Comput. Vis. Pattern Recognit. Workshops (CVPRW)*, Jul. 2017, pp. 136–144.

[26] Y. Zhang, Y. Tian, Y. Kong, B. Zhong, and Y. Fu, "Residual dense network for image super-resolution," in *Proc. IEEE/CVF Conf. Comput. Vis. Pattern Recognit.*, Jun. 2018, pp. 2472–2481.

[27] X. Wang, K. Yu, S. Wu, J. Gu, Y. Liu, C. Dong, Y. Qiao, and C. C. Loy, "ESRGAN: Enhanced super-resolution generative adversarial networks," in *Proc. Eur. Conf. Comput. Vis.* Cham, Switzerland: Springer, 2018, pp. 63–79.

[28] T. Dai, J. Cai, Y. Zhang, S.-T. Xia, and L. Zhang, "Second-order attention network for single image super-resolution," in *Proc. IEEE/CVF Conf. Comput. Vis. Pattern Recognit. (CVPR)*, Jun. 2019, pp. 11065–11074.

[29] *Convolutional Neural Network*. Accessed: Jan. 2020. [Online]. Available: https://www.tensorflow.org/tutorials/images/deep_cnn#convolutional-neuralnetworks

[30] J. Patterson and A. Gibson, *Deep Learning: A Practitioner's Approach*. Newton, MA, USA: O'Reilly Media, Inc., 2017, pp. 72–74.

[31] D. P. Kingma and J. Ba, "Adam: A method for stochastic optimization," 2014, *arXiv:1412.6980*. [Online]. Available: http://arxiv.org/abs/1412.6980

[32] A. L. Maas, A. Y. Hannun, and A. Y. Ng, "Rectifier nonlinearities improve neural network acoustic models," in *Proc. ICML*, 2013, vol. 30, no. 1, p. 3.

[33] M. D. Zeiler and R. Fergus, "Visualizing and understanding convolutional networks," in *Computer Vision—ECCV* (Lecture Notes in Computer Science), vol. 8689, D. Fleet, T. Pajdla, B. Schiele, and T. Tuytelaars, Eds. Cham, Switzerland: Springer, 2014, pp. 818–833.

[34] A. Mahendran and A. Vedaldi, "Understanding deep image representations by inverting them," in *Proc. IEEE Conf. Comput. Vis. Pattern Recognit. (CVPR)*, Jun. 2015, pp. 5188–5196.

[35] S. Ioffe and C. Szegedy, "Batch normalization: Accelerating deep network training by reducing internal covariate shift," 2015, *arXiv:1502.03167*. [Online]. Available: https://arxiv.org/abs/1502.03167

[36] M. D. Zeiler, D. Krishnan, G. W. Taylor, and R. Fergus, "Deconvolutional networks," in *Proc. IEEE Comput. Soc. Conf. Comput. Vis. Pattern Recognit.*, Jun. 2010, pp. 2528–2535.

[37] V. Nair and G. E. Hinton, "Rectified linear units improve restricted Boltzmann machines," *Proc. 27th Int. Conf. Mach. Learn.*, 2010, pp. 807–814.

[38] O. Ronneberger, P. Fischer, and T. Brox, "U-net: Convolutional networks for biomedical image segmentation," in *Proc. MICCAI*, 2015, pp. 234–241.

[39] P. Isola, J.-Y. Zhu, T. Zhou, and A. A. Efros, "Image-to-Image translation with conditional adversarial networks," in *Proc. IEEE Conf. Comput. Vis. Pattern Recognit. (CVPR)*, Jul. 2017, pp. 1125–1134.

[40] X. Mao, Q. Li, H. Xie, R. Y. K. Lau, Z. Wang, and S. P. Smolley, "Least squares generative adversarial networks," in *Proc. IEEE Int. Conf. Comput. Vis. (ICCV)*, Oct. 2017, pp. 2794–2802.

[41] D. Ulyanov, A. Vedaldi, and V. Lempitsky, "Instance normalization: The missing ingredient for fast stylization," 2016, *arXiv:1607.08022*. [Online]. Available: http://arxiv.org/abs/1607.08022

[42] K. He, X. Zhang, S. Ren, and J. Sun, "Identity mappings in deep residual networks," in *Proc. Eur. Conf. Comput. Vis.* New York, NY, USA: Springer, 2016, pp. 630–645.

[43] A. Radford, L. Metz, and S. Chintala, "Unsupervised representation learning with deep convolutional generative adversarial networks," 2015, *arXiv:1511.06434*. [Online]. Available: http://arxiv.org/abs/1511.06434

[44] S. Y. Pang, K. Hirano, R. Fabbro, and T. Jiang, "Explanation of penetration depth variation during laser welding under variable ambient pressure," *J. Laser Appl.*, vol. 27, no. 2, May 2015, Art. no. 22007, doi: 10.2351/1.4913455.

[45] L. Li, G. Peng, J. Wang, J. Gong, and S. Meng, "Numerical and experimental study on keyhole and melt flow dynamics during laser welding of aluminium alloys under subatmospheric pressures," *Int. J. Heat Mass Transf.*, vol. 133, pp. 812–826, Apr. 2019, doi: 10.1016/j.ijheatmasstransfer.2018.12.165.

[46] M. Jiang, X. Chen, Y. Chen, and W. Tao, "Increasing keyhole stability of fiber laser welding under reduced ambient pressure," *J. Mater. Process. Technol.*, vol. 268, pp. 213–222, Jun. 2019, doi: 10.1016/j.jmatprotec.2019.01.026.

[47] J. Ahn, E. He, L. Chen, J. Dear, and C. Davies, "The effect of ar and he shielding gas on fibre laser weld shape and microstructure in AA 2024-T3," *J. Manuf. Processes*, vol. 29, pp. 62–73, Oct. 2017, doi: 10.1016/j.jmapro.2017.07.011.

SEHYEOK OH was born in Seoul, South Korea, in 1991. He received the B.S. degree in mechanical engineering from the Ulsan National Institute of Science and Technology (UNIST), Ulsan, South Korea, in 2014, where he is currently pursuing the combined M.S. and Ph.D. degrees in mechanical engineering. His research interests include application of deep learning to the laser materials processing and mechanical engineering, and industrial application of high-power lasers, such as laser welding, laser cutting, and laser transformation hardening.

HYUNGSON KI received the B.S. degree in mechanical engineering from the Pohang University of Science and Technology (POSTECH), South Korea, in 1996, and the M.S. and Ph.D. degrees in mechanical engineering from the University of Michigan, Ann Arbor, MI, USA, in 1998 and 2001, respectively. He is currently a Professor in mechanical engineering with the Ulsan National Institute of Science and Technology (UNIST), South Korea.

From 2001 to 2003, he was a Postdoctoral Research Fellow with the University of Michigan. From 2003 to 2008, he was an Assistant Professor of mechanical engineering with Michigan State University, East Lansing, MI, USA. His research interests include laser material interaction and processing, multiphysics simulations, and deep learning applications.